Experimental Techniques manuscript No.
(will be inserted by the editor)

Real-time hybrid testing of strut-braced wing under aerodynamic loading using an electrodynamic actuator

V. Ruffini · C. Szczyglowski · D. A. W. Barton · M. Lowenberg · S. A. Neild

Received: date / Accepted: date

Abstract Real-Time Hybrid Simulation (RTHS) is an experimental framework that allows the testing of components or substructures under realistic, dynamic boundary conditions, by imposing the reactions calculated from a model of the rest of the assembly through one or more actuators. In the context of rapid prototyping of mechanical components, RTHS could be used to explore the design space of a device while at the same time physically validating its interaction with other components of the final assembly from the early stages of the design-to-production cycle.

In this work, RTHS was applied for the first time to the investigation of aerodynamic gust loading alleviation devices in a highly flexible strut-braced wing. The model wing was taken as the physical substructure and tested in a low-speed wind tunnel equipped with gust generators. The load alleviation device was simulated through a real-time feedforward-feedback controller, and its response imposed via an electro-mechanical linear actuator, in contrast with the hydraulic actuators more commonly used in standard RTHS.

The controller-actuator subsystem was studied in detail to assess and minimise errors at the physical interface with the wing. The behaviour of the electromechanical subsystem showed a strong dependence on the characteristics of the numerical substructure and the frequency of excitation, and resulted in a significant discrepancy between the simulated and real displacements at the interface between the actuator and the wing. A narrow-band feedforward displacement control scheme based on a model of this subsystem alone was therefore developed and shown to significantly reduce synchronisation errors at the interface.

Keywords Hybrid testing · Cyber-physical testing · Electrodynamic actuators · Control-structure interaction · Aerodynamic loads · Gust loads

1 Introduction

The recent push towards a reduction of the environmental impact of aviation [1] has stimulated research into aircraft architectures capable of delivering not just incremental improvements, but a step change in performance. High aspect ratio (HAR) wings, in particular, have long been recognised as having a significant effect in improving the lift-to-drag ratio and thus fuel efficiency [2]. However, the accompanying increase in the spanwise bending moments has revived interest in the truss-braced wing design [3], where the wing loading is reduced thanks to the additional support of a truss system [4].

Recently, it has been proposed that the truss could serve not simply as static support, but also to reduce dynamic gust loads by inserting a vibration absorber

V. Ruffini
Department of Mechanical Engineering, University of Bristol, Bristol, UK
E-mail: v.ruffini@bristol.ac.uk

C. Szczyglowski
Department of Aerospace Engineering, University of Bristol, Bristol, UK

D. A. W. Barton
Department of Engineering Mathematics, University of Bristol, Bristol, UK

M. Lowenberg
Department of Aerospace Engineering, University of Bristol, Bristol, UK

S. A. Neild
Department of Mechanical Engineering, University of Bristol, Bristol, UK

into one of the struts, either as a traditional suspension system [5], or as an inerter-based device [6]. The geometric nonlinearities stemming from the greater flexibility associated with HAR wings, however, mean that the traditional modelling methods, based on linear elastic and aerodynamic theory, are not necessarily adequate, and can lead to conservative structural designs [7], and to inaccurate estimations of the flutter speeds [3,8]. Wind tunnel testing would therefore be required to validate the performance of a vibration-suppressing device in reducing the loads experienced by the wing in response to dynamic gust loading, especially considering their highly aleatory nature [9], but a thorough experimental exploration of the design space of the absorber would be prohibitively expensive.

Hybrid testing provides an attractive compromise for this application, and will be applied in this work to the investigation of aerodynamic gust loading alleviation devices in a highly flexible strut-braced wing. Within the hybrid testing framework, the structure of interest is divided into a physical substructure, which is subjected to testing, and a numerical substructure, which emulates the behaviour of the rest of the assembly under some chosen excitation [10]. The boundary conditions at the interface between the two are calculated from the model of the numerical substructure, and imposed on the physical substructure through an actuator in real time [11] (hybrid testing is therefore also known as Real-Time Hybrid Simulation (RTHS)).

This method has traditionally allowed to test and validate the dynamics of structures that cannot be systematically studied in a controlled laboratory setting due to their dimensions, such as in earthquake engineering [12–14]. In addition, the technique can also be exploited to quantify the response under realistic loads and boundary conditions of critical components characterised by high levels of uncertainty due to their structural complexity and/or nonlinear behaviour [15,16], or, dually, to assess their effect on the overall assembly [17].

Due to the standard use of hydraulic actuators [18, 19], which are characterised by high output forces, significant effort has been dedicated to minimising the delay they introduce at the interface between numerical and physical substructures [20], as it can lead to potentially destructive instabilities [21]. Several methods have been proposed. One of the most popular is the polynomial forward prediction algorithm [22] with its variants [23], which seeks a least-square best fit of the response of the numerical substructure and uses it to extrapolate into the future and generate a command signal capable of compensating the actuator delay. More recently, feedforward schemes based on models of the specific RTHS set-up have been gaining ground, as they promise higher compensation accuracy [24], wider operational bandwidths [25], and/or to eliminate the risk of instabilities altogether [26].

While these efforts to minimise the experimental errors introduced by RTHS have been concentrated in the civil and — to a smaller extent — mechanical engineering communities, in the past decade RTHS has seen a notable increase in activity from the fields of ocean engineering [27] and fluid-structure interaction (FSI) [28] (where RTHS is more commonly known as *cyber-physical testing*). In these areas, the physical substructure is directly exposed to the real, unknown hydro- or aero- dynamic excitation, while the numerical substructure can be used to simulate a wide range of boundary conditions, especially in terms of stiffness and damping, without the need to build different test specimens. In FSI-related research in particular, this approach has been used extensively for the parametric investigation of complex phenomena for which competitive models of the underlying physics exist, like vortex-induced vibrations in cables and pipes [29,30], energy-harvesting plates [31], or the classical [32] and stall [33] flutter of wings. Contrary to traditional RTHS applications, however, systematic research to quantify the effect of errors and uncertainties in the hybrid set-up on the fidelity of the test outcome began only recently [34–36].

This work aims therefore at bringing together the new focus on light-weight aeroelastic structures with the standard RTHS practice of rigorous treatment of the errors introduced by the actuation system. In this paper, a typical RTHS set-up will be applied to the parametric exploration of the design space of a vibration absorber for a strut-braced wing. A compensator for the actuation system based on an inverse model of the electro-mechanical system alone, and its robustness to uncertainty, will be presented. Particular attention will be devoted to the influence of the numerical substructure on the frequency characteristics of the response of the physical substructure and of the compensator. Finally, the approach will be verified with wind tunnel tests on a model strut-braced wing using a narrow-band implementation of the compensator.

The set-up described above presents three significant novelties with respect to traditional hybrid testing, which bring it closer to cyber-physical applications: i) the excitation to the physical substructure is not imposed via the actuator together with the calculated boundary conditions, but comes from a gust generator installed inside the Large low-speed Wind Tunnel (LWT) at the University of Bristol, and is therefore unknown; ii) the actuator used is not hydraulic, but an electrodynamic shaker better suited to the lightweight

structures found in sub-scale experimental aerospace applications; iii) the characteristics of the numerical substructures are not fixed at the beginning of the test campaign, but can vary significantly in order to span the design space of the device.

2 Real-time dynamic substructure testing

2.1 System overview

Fig. 1 illustrates the main components of the RTHS set-up used in this work. A simplified model of a strut-braced wing was taken as the physical substructure and installed inside the LWT. This allowed its aeroelastic behaviour to be studied without modelling approximations [37] and under real operational conditions, and to directly observe any effects arising from the interaction between geometric nonlinearities and the airflow, for which reliable modelling tools are still being actively researched [38,39].

The numerical substructure simulates the presence of a vibration-suppressing device at the root of the strut, where the strut would be joined to the airframe. The dynamic boundary conditions (displacements in this case) that would be generated by the interaction between the wing-strut substructure and the device are imposed by an actuator. These boundary conditions are calculated in real time by feeding the force measured at the interface between the strut and the actuator into the model of the damping device, and obtaining the corresponding instantaneous displacement. This numerical displacement is then used as the reference signal for the control system that drives the actuator.

The control system is traditionally split into two stages. The first is the servo-drive for the actuator, which is usually a proprietary PID controller that takes care of basic position tracking and offers additional safety features. The second is wrapped around the servo-drive, and acts as a feedforward compensation of the dynamics of the actuator. This latter element is of crucial importance for hybrid testing, as the compensator has to ensure near-perfect synchronisation between the physical and the numerical displacement at the interface between the two substructures. It is well known in the hybrid testing literature that delays between numerical and physical displacements can lead to instabilities [22,40], but a mismatch also means that the dynamics of the real assembly are not accurately reproduced [36].

2.2 Hybrid testing implementation

The block diagram of the actual implementation of the system is shown in Fig. 2. The wing-strut substructure H is excited by the aerodynamic external force F_e, and the force measured at the interface between the actuator A and H is sent to a block that contains the model of the numerical substructure (N). The feedforward compensating algorithm P then calculates the reference displacement signal D_c for the PID-based servo-drive by passing the numerical displacement D_n through an inverse model of the electro-mechanical system (capitalised letters correspond to variables in the Laplace domain).

The servo-drive comprises a PID loop for position control (C_d), which takes as inputs D_c and the measured actuator displacement D_a and generates a control force F_c. The position loop is followed by a PI current control loop (C_F), which takes the error between F_c and the actual force imposed by the actuator and produces the voltage V necessary to drive the actuator. The actuator force is obtained indirectly within the controller itself by multiplying the measured current I by the motor constant k_I, and represents therefore its electromagnetic component. The actuator, subjected to the interface force F_m and V, finally generates the displacement boundary condition D_a at the interface as output.

Since a strong interaction between mechanical, electrical, and digital components was expected, a model of the whole system was developed in order to investigate the influence of these elements on RTHS control and accuracy. Particular focus will be put on the subsystem comprising the actuator, servo drive, and numerical substructure, which will be henceforth referred to as the electro-mechanical subsystem.

2.3 Model of the electrodynamic actuator

The electrodynamic actuator used in this work consists of a permanent magnet and a current-carrying coil that moves due to the Lorentz force generated by the interaction between current and electromagnetic field. The actuator was modelled mechanically as a single-degree-of-freedom oscillator characterised by mass m_a, viscous damping c_a, and stiffness k_a, and electrically as an equivalent RL circuit [41] with inductance L_a and resistance R_a, according to Eqs. (1) (lower-case letters indicate variables in the time domain):

$$\begin{cases} m_a\ddot{d}_a(t) + c_a\dot{d}_a(t) + k_a d_a(t) = k_I i(t) + f_m(t) \\ k_I\dot{d}_a(t) + L_a\dot{i}(t) + R_a i(t) = v(t). \end{cases} \quad (1)$$

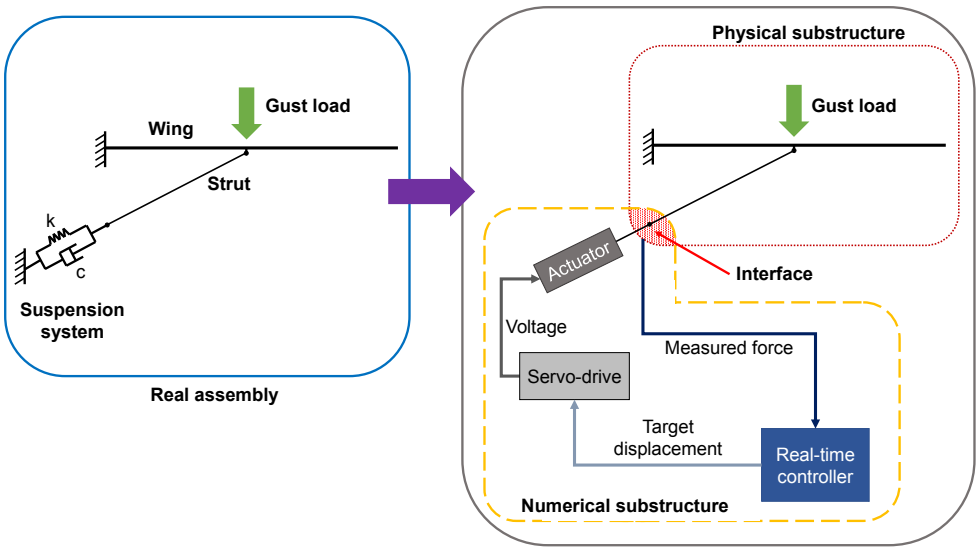

Fig. 1 Schematic overview of real-time hybrid testing.

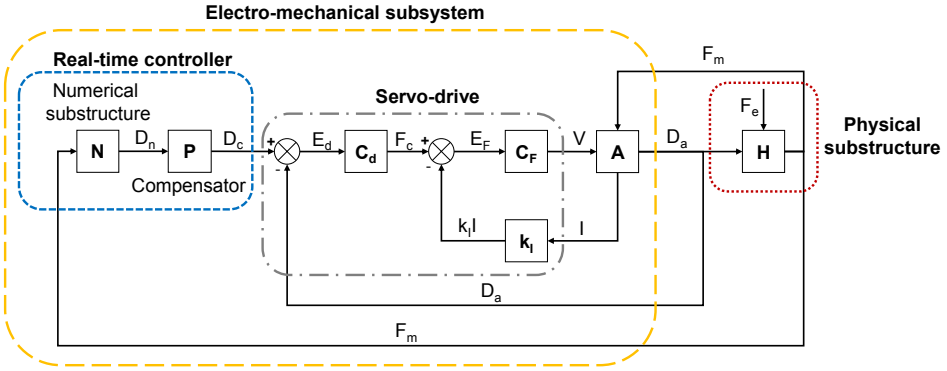

Fig. 2 Block diagram of the displacement control implementation.

The actuator is subjected to the force $f_m(t)$ at the interface with the physical substructure and to the electromagnetic force, which is proportional to current $i(t)$ through the motor constant k_I. On the electrical side, $k_I \dot{d}_a(t)$ is the back-electromagnetic force, and $v(t)$ the voltage supplied by the servo-drive. Switching to the Laplace domain, it is possible to express Eqs. (1) in transfer function form, which will make for a more convenient derivation of the global model, as follows

$$A_m D_a = k_I I + F_m \tag{2}$$

$$A_{mI} D_s + A_I I = V, \tag{3}$$

where the capitalised letters indicate Laplace transforms of the time-domain variables in Eqs. (1). The transfer functions A_m, A_I, and A_{mI} are expressed as

$$A_m = m_a s^2 + c_a s + k_a$$
$$A_I = L_a s + R_a$$
$$A_{mI} = k_I s,$$

with s the Laplace complex frequency variable.

2.4 Model of the control system

As stated in Sect. 2.2, the servo-drive implements a two-stage control system. The first is a PID position control loop in parallel form. Its input passes first through a Butterworth low-pass (LP) filter with cut-off frequency ω_1, and the overall transfer function C_d can be expressed as

$$C_d = \frac{\omega_1}{s + \omega_1} \left(k_p + k_d s + \frac{k_i}{s} \right), \tag{4}$$

where k_p, k_d and k_i are the proportional, derivative and integral gains for the position loop, respectively. The output of the position loop is the target force F_c necessary to achieve the reference displacement D_c, and can therefore be written as

$$F_c = C_d E_d = C_d \left(D_c - D_a \right), \tag{5}$$

where E_d is the error between the reference displacement and the actual displacement D_a of the actuator.

The second stage is a PI current control loop, also in parallel form. Its input is filtered by a second LP filter with cut-off frequency ω_2, and the resulting transfer function C_F is

$$C_F = \frac{\omega_2}{s+\omega_2}\left(k_{Fp} + \frac{k_{Fi}}{s}\right), \tag{6}$$

where k_{Fp}, k_{Fi} are the proportional and integral gains for the current loop. Its output is the supply voltage V to the actuator

$$V = C_F E_F = C_F\left(F_c - k_I I\right), \tag{7}$$

which is proportional to the error E_F between the target force F_c and the electromagnetic force $k_I I$.

2.5 Numerical substructure

The numerical substructure simulates a vibration suppressing device that in this work takes the form of a simple coilover-like suspension system. The mass of the device is incorporated in the physical substructure through the actuator pushrod (see Sect. 4.1), and the model of the simulated device is therefore

$$c_n \dot{d}_n + k_n d_n = f_n, \tag{8}$$

where c_n is the viscous damping coefficient and k_n the stiffness of the numerical substructure. The force f_n is the interface reaction acting on the simulated device and, in the case of displacement control, is the input to the numerical subsystem; therefore, in the present case, it coincides with the measured force f_m.

Moving to the Laplace domain and assuming $F_n = F_m$, Eq. (8) can be written as

$$D_n = \frac{F_m}{c_n s + k_n} = N F_m, \tag{9}$$

where N represent the transfer function associated with the numerical substructure.

2.6 Physical substructure

The physical substructure is a sub-scale strut-braced HAR wing (AR 17 — more details on the wing geometry can be found in Sect. 4.1). As can be seen in Fig. 2, the substructure H is treated as a multiple-input single-output system. It is subjected to the external, unknown aerodynamic force F_e, and to the displacement constraint d_a imposed by the actuator at the strut root. The resulting reaction force F_m at the interface with the actuator is the output, and summarises the entirety of the interaction between the numerical and physical substructures. For this reason, and because model validation is beyond the scope of this paper, a detailed analytical model of the wing will not be presented. In addition, as will be shown in Sect. 3.2, an expression for the compensator P will be sought with the explicit aim of avoiding any form of system identification of H prior to commencing the hybrid testing of the physical substructure.

3 Effect of the electro-mechanical subsystem on real-time performance

3.1 Influence of the numerical substructure

In standard hybrid testing, the design of the inner and outer control loops defined in sect. 2.2 is dominated by the need to compensate for the dynamics of the heavy-duty hydraulics actuators necessary in the civil engineering field, and by the characteristics of the physical substructure, often a vibration-suppressing device, while the numerical substructure is usually a lightly damped system.

These premises, however, are inverted in the present work, as the physical substructure (the wing) has relatively low damping with respect to the numerical substructure, which simulates the vibration-suppressing device. In addition, since hybrid testing in this work was used as a means of exploration of the design space of the device, the stiffness and damping of the numerical substructure were varied significantly during the test campaign. For these reasons, the effects of the parameters of the numerical substructure on the behaviour of the system were studied in detail.

As the need for a hybrid test presupposes, in general, the lack of an accurate model of the system, the most reliable way to assess its accuracy is to compare the displacements of the numerical (D_n) and physical (D_a) substructures, because their coincidence ensures that the boundary conditions have been realistically enforced. An expression for their ratio was therefore sought. By combining Eqs. (2)-(7) and deriving $F_m = N^{-1} D_n$ from Eq. (9), it is possible to obtain an expression for D_a/D_n that excludes the unknown dynamics of the physical substructure, and can be expressed as

$$\frac{D_a}{D_n} = \frac{k_I\, C_F\left(C_d\, P\, N + 1\right) + A_I}{\left(k_I\left(\left(A_m + C_d\right) + A_m\, A_I\right) N\right.}. \tag{10}$$

As expected, Eq. (10) depends on the electro-mechanical dynamics of the actuator, on the characteristics of the

Table 1 Parameters of the electro-mechanical subsystem

Mechanical		
Mass (kg)	m_a	2.7
Stiffness (N/m)	k_a	10
Viscous damping (kg/s)	c_a	2
Electrical		
Inductance (H)	L_a	0.025
Resistance (Ω)	R_a	1.6
Motor constant (N/A)	k_I	20.1
Servo-drive		
Position P gain (N/mm)	k_p	49
Position I gain (N/(mm s))	k_i	39
Position D gain (N s/mm)	k_d	0.39
Current P gain (V/N)	k_{Fp}	0.07
Current I gain (V/(N s))	k_{Fi}	0
Position LP filter cut-off frequency (rad/s)	ω_1	28274
Current LP filter cut-off frequency (rad/s)	ω_2	628

displacement and current controller and of the numerical substructure, and on the compensator P, if any. It is important to note, however, that the relative behaviour of the numerical displacement and the physical displacement of the actuator are entirely independent of the physical substructure.

Fig. 3 shows the Bode plots of D_a/D_n for various combinations of numerical substructure parameters k_n and c_n, with k_n varying between 100 and 10,000 N/m, and c_n between 10 and 1,000 kg/s. Here, the compensator P was assumed to be a unit gain in order to isolate the influence of the numerical substructure. Likewise, the parameters of the PID/PI controller and of the actuator dynamics were kept constant at the values summarised in Table 1. The mechanical and electrical parameters, with the exception of m_a and k_I, which were supplied by the manufacturer, were identified experimentally by feeding a stepped-sine signal through the servo-drive to the actuator, and deriving the transfer function between the command and measured displacements. The particle swarm optimisation algorithm [42] was then used to find the values minimising the difference between the experimental transfer function and Eq. (10).

It can be seen that, while D_a/D_n does not change significantly when varying the numerical stiffness k_n, damping parameter c_n has a major effect. The gain plot shows that, without compensation, the actual displacement of the actuator would be 13 times as large as the target displacement with $c_n = 1000$ kg/s, and 5 times as large with $c_n \leqslant 300$ kg/s. The effect on the relative phase is even more important, and here can result in the physical displacement D_a *leading* the numerical displacement D_n depending on the value of numerical damping — something that, to the authors' knowledge, has not previously been reported in the literature. In particular, D_a leads D_n over the whole 0–15 Hz frequency range at high damping values ($c_n \geqslant 1000$ kg/s), while for ($300 \leqslant c_n < 1000$ kg/s) the behaviour changes from D_a leading D_n to D_a lagging D_n at higher frequencies. At lower damping values, on the other hand, D_a lags D_n at all frequencies, but the time shift is markedly frequency-dependent, and thus cannot in general be approximated as a pure delay.

3.2 Lead-lag compensation

As shown in Fig. 3, a hybrid testing set-up with no compensation for the dynamics of the transfer system would lead to a very poor reproduction of the interface boundary conditions, and potentially dangerous operation. Considering the additional issue of the lead-lag behaviour highlighted in the previous section, an analytical expression for an ideal compensator was sought, by requiring Eq. (10) to equal 1, i.e. imposing a perfect match between D_a and D_n, and solving for P. The ideal compensator P_{id} can then be written as

$$P_{id} = \frac{1}{k_I\, C_F\, C_d\, N}\big(k_I\,(((A_m + C_d)\, C_F + A_{mI})\, N - C_F) + A_I\,(A_m N - 1)\big). \quad (11)$$

It can be seen that P_{id} in this experimental configuration needs to compensate not only for the dynamics of the actuator, but also for the stabilising servo-drive and the numerical substructure. The advantage of Eq. (11) over similar approaches based on the identification of the global system [24,43] is that P_{id} requires no knowledge or testing of the physical substructure, as it depends only on deterministic parameters (C_d, C_F, N), and the characteristics of the actuator (see Table 2), which can usually be identified to a smaller degree of uncertainty with respect to the physical substructure. For the same reasons, the approach can be applied equally to linear and nonlinear physical substructures.

Fig. 4 shows the amplitude and phase values of P_{id} for $k_n = 8000$ N/m and $c_n = 200$ kg/s and compares them with D_a/D_n. It is apparent that, while the presence of the compensator is meant to eliminate the lead/lag between D_a and D_n, the synchronising time shift imposed by the compensator is *not* in general related to this lead/lag. It is particularly striking, in this sense, that the physical actuator displacement D_a leads the numerical one D_n up to 11 Hz and starts lagging at higher frequencies, but the compensator always prescribes a lag for the command signal to the actuator.

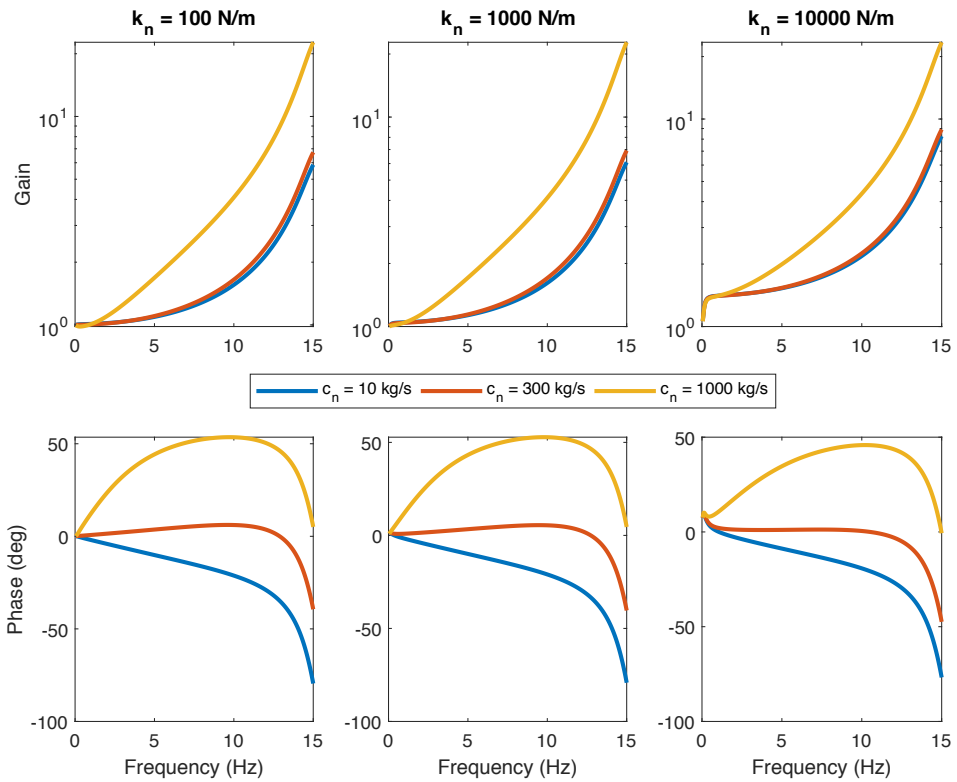

Fig. 3 Influence of numerical substructure on the lead/lag behaviour of the controller-actuator subsystem

Table 2 Coefficients of the ideal compensator P_{id}

Order	Coefficient
	Numerator
s^7	$L_a m_a$
s^6	$((\omega_1+\omega_2)m_a + c_a - c_n)L_a + R_a\, m_a$
s^5	$((m_a\,\omega_1 + c_a - c_n)\omega_2 + (c_a - c_n)\omega_1 + k_a - k_n)L_a + m_a\,(k_I\,k_{Fp} + R_a)\omega_2 + R_a\,m_a\,\omega_1 + (c_a - c_n)R_a + {k_I}^2$
s^4	$((R_a\,m_a + (c_a - c_n)L_a + k_I\,k_{Fp}\,m_a)\omega_1 + (c_a - c_n)R_a + (k_a - k_n)L_a + k_I\,(c_a\,k_{Fp} - c_n\,k_{Fp} + k_{Fi}\,m_a + k_I))\omega_2 +$ $+((c_a - c_n)R_a + (k_a - k_n)L_a + {k_I}^2)\omega_1 + R_a\,(k_a - k_n)$
s^3	$(({k_I}^2 + ((k_d + c_a - c_n)k_{Fp} + k_{Fi}\,m_a)k_I + (c_a - c_n)R_a + (k_a - k_n)L_a)\omega_1 + ((k_a - k_n)k_{Fp} + k_{Fi}\,(c_a - c_n))k_I +$ $+R_a\,(k_a - k_n))\omega_2 + \omega_1\,R_a\,(k_a - k_n)$
s^2	$\omega_2\,((((k_d + c_a - c_n)k_{Fi} + k_{Fp}\,(k_p + k_a - k_n))k_I + R_a\,(k_a - k_n))\omega_1 + k_I\,k_{Fi}\,(k_a - k_n))$
s	$k_I\,\omega_1\,\omega_2\,((k_p + k_a - k_n)k_{Fi} + k_{Fp}\,k_i)$
s^0	$k_I\,k_{Fi}\,k_i\,\omega_1\,\omega_2$
	Denominator
s^3	$k_I\omega_1\omega_2 k_d k_{Fp}$
s^2	$k_I\omega_1\omega_2\,(k_{Fi}k_d + k_{Fp}k_p)$
s	$k_I\omega_1\omega_2\,(k_{Fi}k_p + k_{Fp}k_i)$
s^0	$k_I k_{Fi} k_i \omega_1 \omega_2$

An explicit expression therefore allows a quick calculation of the compensator for a wide range of numerical parameters. However, the ideal predictor P_{id} results in an improper transfer function, where the numerator is a polynomial of order 7 in the Laplace variable s, and the denominator is of order 3. Its practical implementation is therefore challenging, as P_{id} tends to behave as a differentiator at high frequencies, thus strongly amplifying noise. To bypass this issue, the compensator was calculated offline, and implemented as a look-up table in the form of an amplitude adjustment factor and a lead/lag value for the command signal D_c depending on the values of the forcing frequency. This approach is valid because the wing, despite being geometrically nonlinear due to its high flexibility, exhibited a response to both continuous and transient gusts that could very

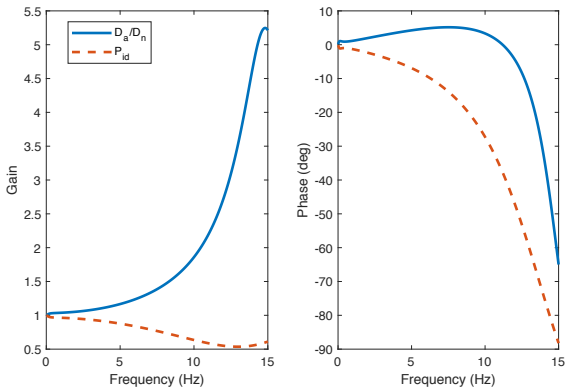

Fig. 4 Bode plot of ideal compensator P_{id} for displacement control, $k_n = 8000$ N/m, $c_n = 200$ kg/s, compared with the transfer function D_a/D_n between physical and numerical displacement at the interface.

closely be approximated as single-frequency. A broadband implementation of Eq. (11), on the other hand, would be necessary to fully compensate for a nonlinear physical substructure characterised by a significantly multi-harmonic behaviour.

3.3 Effect of compensation on test accuracy

As P_{id} depends on the mechanical and electrical characteristics of the actuator, which were identified experimentally on the real system, an analysis was conducted to assess the effect of their uncertainty on the overall accuracy of the hybrid test results.

While the uncertainties can be assessed using estimates from system identification techniques, practical experience suggests that these are often underestimates when other factors such as environmental changes (which might be negligible during a single test, but significant over a test campaign) are considered. As such, the variables m_a, c_a, k_a, L_a, R_a, and k_I were assigned indicative interval errors based on past experience of such time-dependent changes of ±5%, ±25%, ±5%, ±2.5%, ±10%, and ±1% of their nominal values, respectively. Assuming a uniform distribution, these intervals were sampled using the Latin hyper-cube technique, and the values were used to calculate P_{id}.

Fig. 5 shows the range of the gain and phase for the resulting P_{id}, based on 10,000 sample vectors of the uncertain variables. For the sake of conciseness, only the case for $k_n = 8000$ N/m and $c_n = 800$ kg/s will be shown, but it should nevertheless be noted that the numerical substructure significantly affects the behaviour of the compensator with respect to uncertainty as well.

The uncertainty increases with frequency both on the gain and phase. The effect on the accuracy at the interface is shown in Fig. 6. It can be seen that, in the worst case, an inaccurate compensator can cause the ratio of actuator displacement D_a to be as large as 3.3 times, or well below 0.01, the theoretical value D_n. Similarly, D_a can be made to lead or lag D_n by ±180° at frequencies higher than 11.6 Hz, which could potentially force the system outside of its stability margins.

These results show that, to maximise accuracy at the interface between numerical and physical substructures, an adaption scheme [23,44] or an additional feedback loop [24] is necessary to obtain the correct values of the gain and phase of the compensator. However, it can also be seen that, with no compensation, the error on the amplitude of D_a would be of 1280%, and D_a and D_n could be out of phase by as much as 38° at 10 Hz. This suggests that even a non-optimal compensator yields a more accurate interface behaviour, at least in the lower frequency range.

4 Experimental verification

4.1 Experimental set-up

The experimental set-up is shown in Fig. 7. As discussed in Sect. 2.1, a model of a strut-braced wing was taken as the physical substructure, so that it could be directly subjected to realistic aerodynamic excitation within the LWT. The wing consists of a central spar in 6082T6 aluminium (1300 mm × 50 mm × 4 mm), while the aerofoil (NACA0018, 150 mm chord, span 1.2 m) is made of laser-cut styrofoam to minimise non-structural mass, and reinforced at the trailing edge by thin aluminium tape (Fig. 8). The wing is mounted horizontally inside the LWT, which is a recirculating low-speed wind tunnel with a test section of 2.14 m × 1.525 m by 3.235 m in length and maximum airspeed of 64 m/s.

The strut is a 735 mm-long aluminium rod with a diameter of 12 mm, and is connected to the wing through a SKF SIL8C rod end with a PTFE-lubricated plain spherical bearing. At its root, the strut is attached via a second rod end to a steel push-rod. This push-rod works as the link between the strut, which must be exposed to the airflow, and the actuator, which is cradled in a trunnion outside of the wind tunnel. The push-rod is supported through a linear ball bearing (KBS, model LMF12L) mounted on the trunnion, to stiffen the connecting structure, with minimal added friction, and avoid spurious resonances not associated with the physical substructure proper. The push-rod is bolted to the armature through a LORD MIN811-250LBTC-125

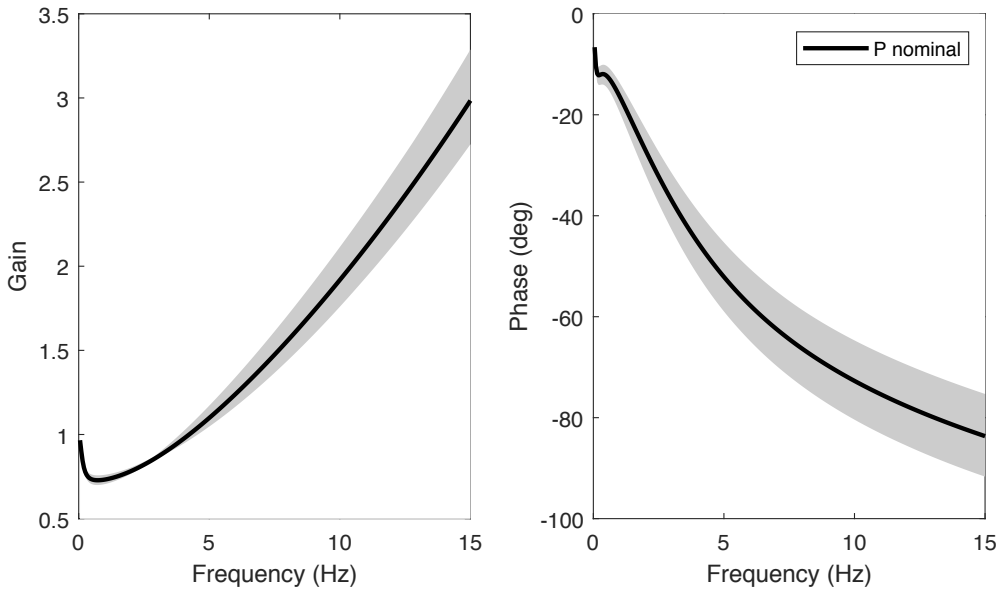

Fig. 5 Bode plot of ideal compensator P_{id} for displacement control when subject to uncertainty on the parameters of the electro-mechanical subsystem ($k_n = 8000$ N/m, $c_n = 800$ kg/s).

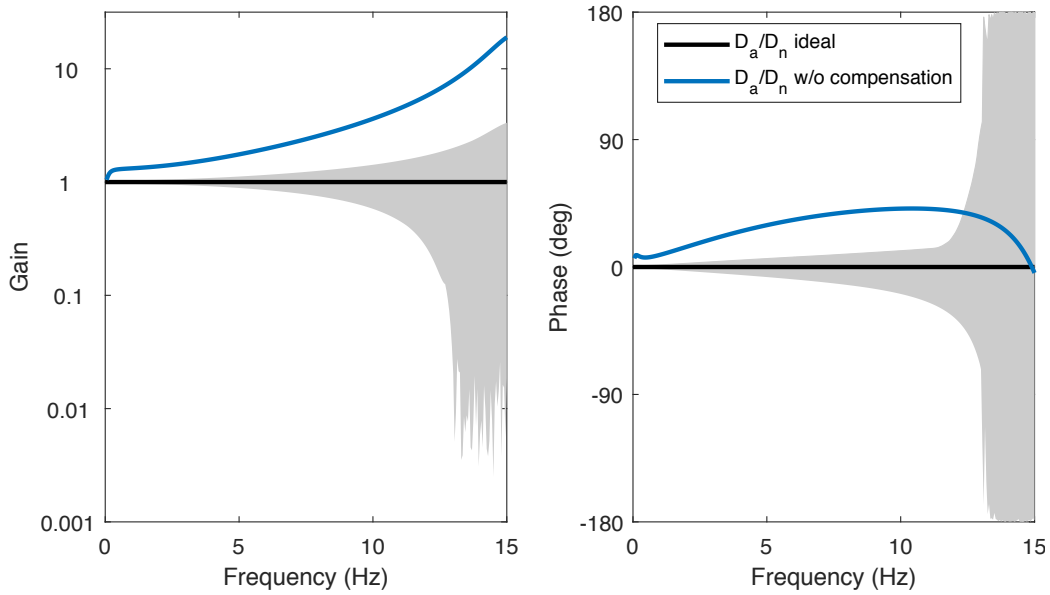

Fig. 6 Effect of the uncertainty of the compensator on $\frac{D_a}{D_n}$ ($k_n = 8000$ N/m, $c_n = 800$ kg/s)

load cell (1.2 N accuracy), which measures the force exchanged at the interface between physical substructure and actuator.

The actuator is an APS 400 Electro-Seis long-stroke electrodynamic shaker, with a peak-to-peak displacement of 158 mm, maximum force of 400 N, and frequency range of 0–100 Hz. The displacement of the actuator armature is controlled by a digital servo-drive (Ingenia Pluto 8/48): it implements a PID position control loop running at 1 kHz, followed by a PI current control loop running at 10 kHz, which adds current-limiting safety features.

The displacement of the actuator is measured by an Acuity® AR500-250 laser triangulation distance sensor with a sampling frequency of 9400 Hz (linearity ±0.375 mm, resolution 0.025 mm). Due to the high axial stiffness of the push-rod, it is assumed that the dis-

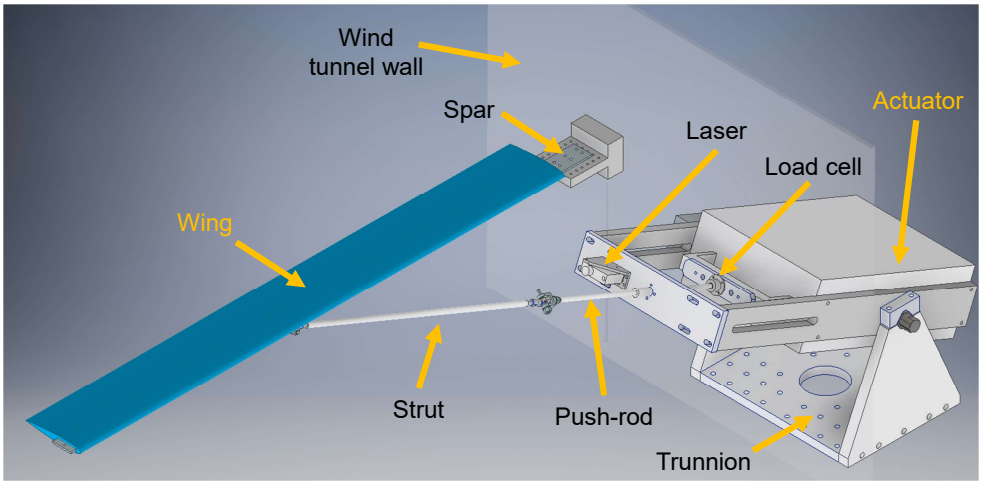

Fig. 7 Test rig lay-out.

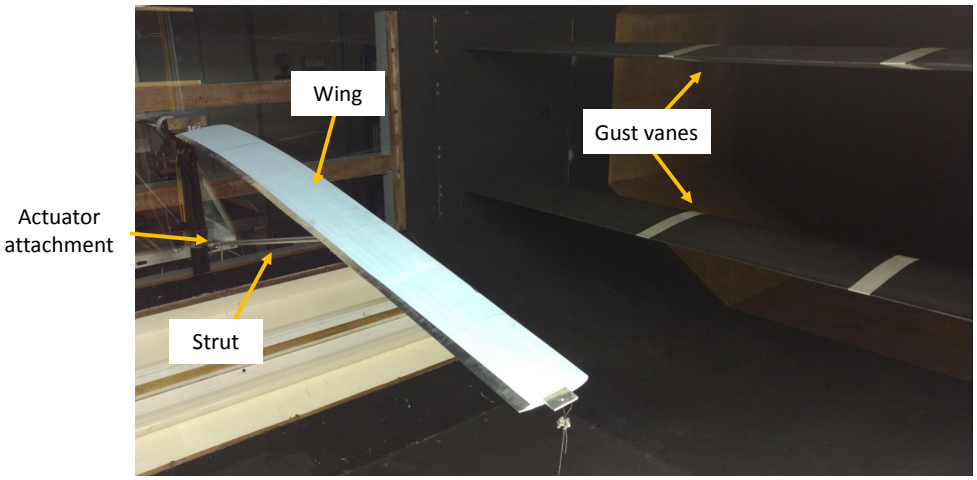

Fig. 8 Test rig: Wing and gust vanes.

placement of the actuator coincides with the displacement at the root of the strut.

As stated in Sect. 2.2, the dynamic excitation of the system was generated on the physical substructure side by a pair of gust vanes [45] (Fig. 8). They consist of two wings driven by two synchronised electrical motors programmed to follow a 1-cosine trajectory, with the instantaneous pitch angle θ of the wings expressed as:

$$\theta = \frac{A_\theta}{2}\left(1 - \cos(2\pi f_\theta t)\right)$$

The user can set the peak-to-peak rotation amplitude A_θ (maximum 20° pk-pk), and the frequency f_θ of the gusts (0.1–15 Hz) at the beginning of the test, after which the vanes can generate either a continuous gust train, or a single gust. Both modes were used during the test campaign, to verify both the steady-state and transient performance of the proposed hybrid testing set-up.

4.2 Outer-loop controller implementation

The displacement and force signals were both acquired by a NI 9215 16-bit analog input module hosted in a cRIO-9035 controller. The cRIO is an embedded controller comprising a Kintex-7 70T FPGA and a dual-core processor running the NI Linux Real-Time OS.

The FPGA was used to run the operations associated with the numerical substructure in real time, i.e. the integration of the force signal acquired by the load cell (Eq. (8)) and the calculation of the reference signal to the actuator through the compensator. To maximise computational speed and accuracy, an exponential integrator scheme matching the exact discretisation of

Eq. (8) was chosen [46], and the instantaneous value of displacement d_n of the numerical substructure at time $t_{k+1} = (k+1)\Delta t$ was calculated as

$$d_n[k+1] = \mathrm{e}^{-\frac{k_n}{c_n}\Delta t} d_n[k] - \frac{(\mathrm{e}^{-\frac{k_n}{c_n}\Delta t} - 1)}{k_n} f_m[k], \qquad (12)$$

where Δt is the sampling time, and k indicates the current discrete time step.

The real-time OS was used for less time-critical or non-deterministic tasks, such as the determination of the compensator parameters. The time lead/lag compensation value corresponding to the excitation frequency f_θ was retrieved from the look-up table presented in Sect. 3.2. Lead compensation requires the forward prediction of the command signal d_c. Here, a standard least-squares polynomial extrapolation algorithm [23] was applied, which uses a least-square polynomial fit of the numerical displacement d_n up to current time step t_k and projects it n steps forward in time. In the case of a lag, which means the command signal d_c reduces to the numerical displacement d_n delayed by the lag, d_c was simply retrieved from a circular buffer of d_n, updated at each time step Δt. The case selection and calculation of the gains of the predictor were performed in the real-time OS, while the actual calculation of d_c was implemented in the FPGA for maximum computational speed.

With this configuration, the numerical substructure simulation could be run at 4 kHz ($\Delta t = 0.25$ ms) as opposed to the 500 Hz feasible on the real-time OS, which allowed the minimisation of the computational delay, and a smoother control action. The reference signal to the servo-drive was then generated by a NI 9263 16-bit analog output module.

4.3 Wind tunnel tests

The procedure for the wind tunnel tests is as follows. The angle of attack of the wing was kept at 2° throughout the experimental campaign, and the numerical parameters k_n and c_n were set at the beginning of each test, and the real-time controller switched on. The airspeed gradually increased from 0 to 20 m/s (maximum Reynolds number $Re = 200,000$), at which point the gust vanes were activated, with a constant amplitude $A_\theta = 8°$. In continuous mode, the excitation frequency f_θ of the gust vanes was kept constant for 40 s and then incremented, as in a stepped-sine test, from 1 Hz to a maximum of 15 Hz.

Fig. 9a shows the measured displacement of the actuator, both numerical and experimental, across the duration of a whole test, for $k_n = 8000$ N/m and $c_n = 800$ kg/s, with the compensator turned off. The discrepancy between the amplitude of numerical displacement d_n and physical displacement d_m is obvious at all frequencies. It should also be noted, however, that the system can accurately follow the quasi-static position drift due to the lift increasing with airspeed without any additional corrective factors, thanks to the integral gain in the position control PID.

In Fig. 9b, the response at 5 Hz is shown as an example, and it can be seen that, in addition to the amplitude error, the physical displacement leads the numerical by 17 ms (corresponding to 31°). Fig. 9c shows d_n and d_a at 5 Hz with the compensator on, which provides an amplitude adjustment factor of 1.15 and an added lag of 29 ms (52°). It is apparent that the lead is completely cancelled, and the amplitude error has been drastically reduced.

The accuracy of the hybrid test at the interface between numerical and physical substructures across the 1-15 Hz frequency range is summarised in Fig. 10, for the case $k_n = 8000$ N/m and $c_n = 800$ kg/s. It can be seen in Fig. 10a that the actual values of the amplitude and phase of the compensator that yield minimal error in D_a/D_n are very close to the the ones predicted by the model for P_{id}. As a result, the amplitude error at the interface is 2.3% on average, while without compensation it would vary from 49% at 1 Hz to 400% at 11 Hz.

The lead between D_a and D_n is reduced from a shift of 38° to 1° up to 8 Hz. From 8 to 11 Hz, it can be seen that the error tends to increase, although staying below the uncompensated value, up to 20° at 11 Hz. This is reasonable, since, as shown in Fig. 6, the response is more sensitive to errors in the compensator at frequencies larger than 10 Hz. In addition, the 10–13 Hz range is dominated by an edgewise mode of the wing, where the wing vibrates in the direction of the chord, perpendicular to the strut, thus limiting the efficacy of the control action. It should also be noted that no hybrid test data is reported at frequency higher than 11 Hz because the amplitude of D_a fell below the resolution of the PID controller.

To assess the impact of these boundary condition errors on the performance of the hybrid test, the transfer function N of the emulated vibration-suppressing device as obtained from RTHS was compared to its theoretical counterpart from Eq. (9) (Fig. 11). The amplitude of the experimental N matches closely the theoretical values (Fig. 11a). The phase (Fig. 11b) also matches well up to 8 Hz, after which the discrepancies between experimental and theoretical values mirror those in the interface displacements shown in Fig. 9c. Without compensation, on the other hand, the behaviour of the em-

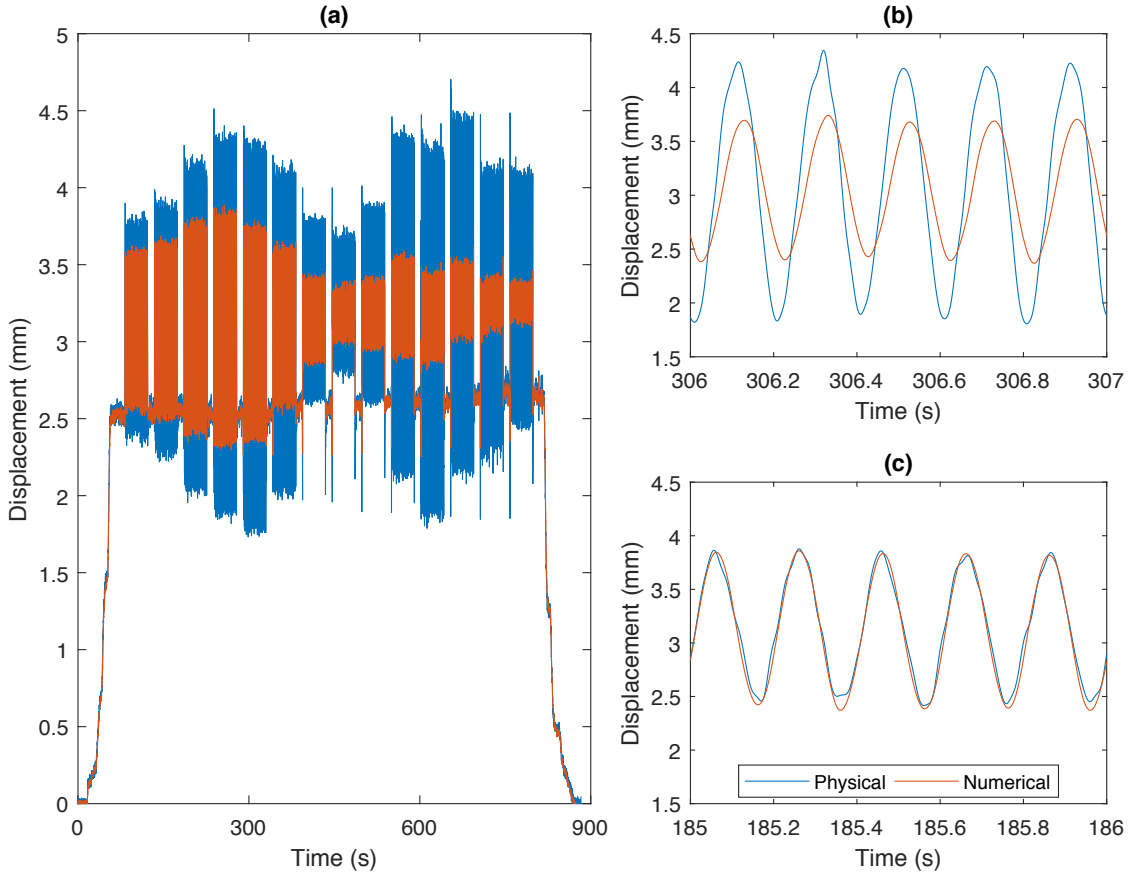

Fig. 9 Time-domain response to gust train, physical and numerical displacements at the strut root, with $k_n = 8000$ N/m, $c_n = 800$ kg/s: a) at different frequencies (1–15 Hz), without compensation; b) at 5 Hz, without compensation; c) at 5 Hz, with compensation.

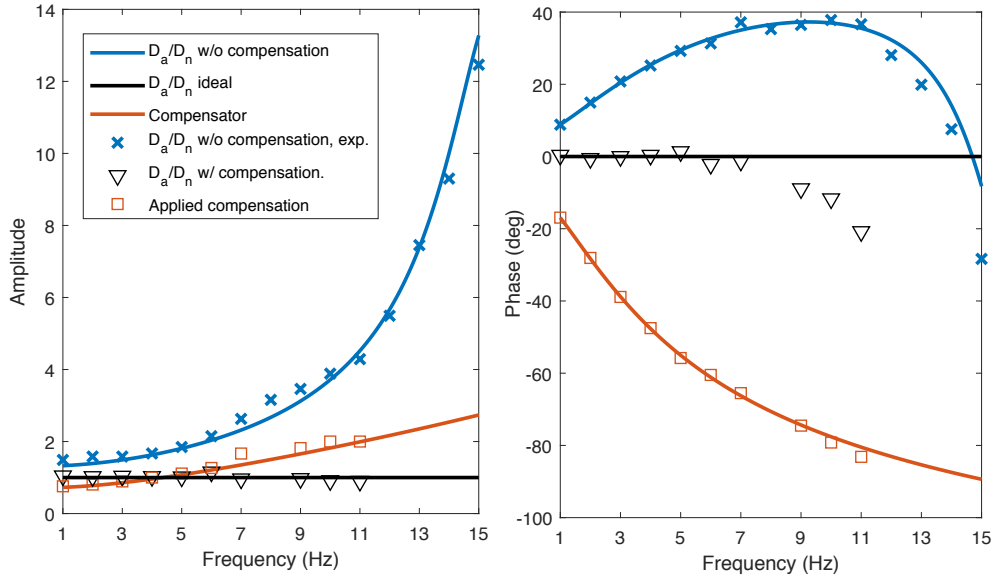

Fig. 10 Comparison between analytical and experimental values of D_a/D_n with and without compensation, and of the compensator P_{id}.

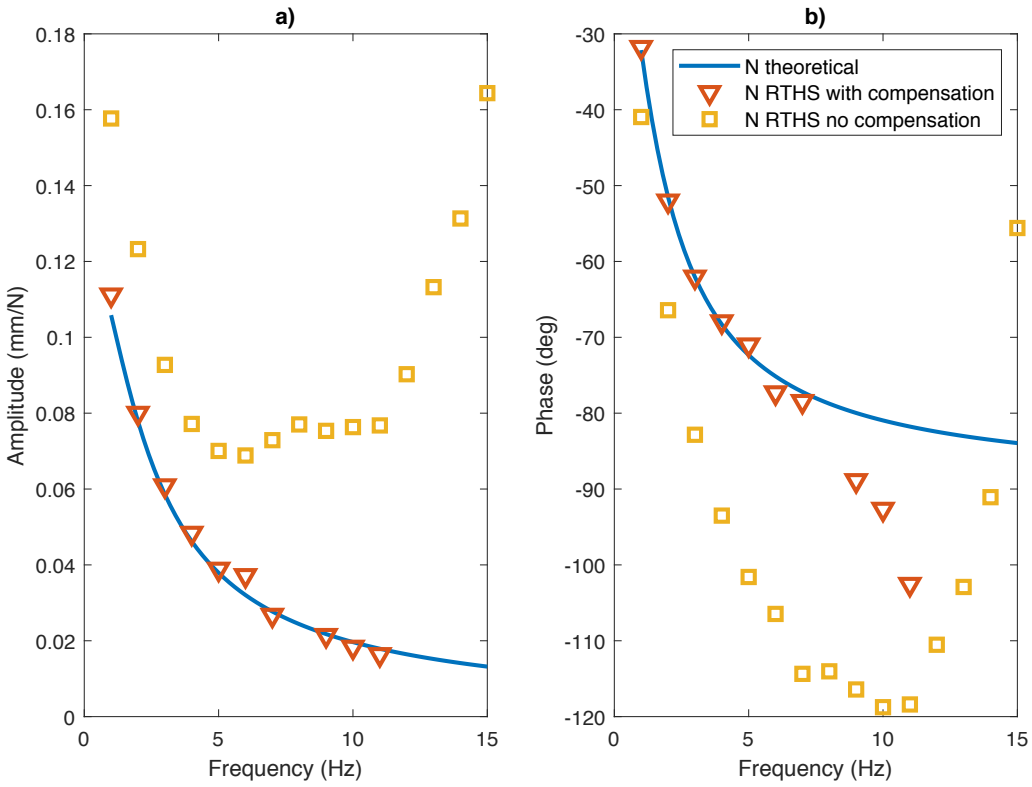

Fig. 11 Comparison of the output of the simulated vibration suppression device transfer function N between the purely theoretical system (Eq. (9)) and the RTHS results for the cases where the proposed compensator P_{id} is used and where no compensator is included ($k_n = 8000$ N/m, $c_n = 800$ kg/s).

ulated device within the RTHS differs from that of a spring-damper system across the entire frequency range of interest.

Fig. 12 shows the displacements resulting from isolated 5-Hz gusts for different combinations of k_n and c_n spanning the design space of the vibration-suppression device: the first row (Figs. 12a and 12b) correspond to the softest spring simulated ($k_n = 100$ N/m), while the second (Figs. 12c and 12d) to the stiffest ($k_n = 8000$ N/m). Likewise, the first column corresponds to the lowest value of numerical damping c_n used in the RTHS tests ($c_n = 200$ kg/s), and the second to the largest ($c_n = 800$ kg/s). In all cases, there is very close agreement between d_n and d_a, indicating a good performance of the compensator for this kind of transient excitation dominated by a single frequency. The simulated suspension system has a noticeable effect on the gust response, with a reduction in the peak displacement of 64% with $k_n = 100$ N/m and 36% with $k_n = 8000$ N/m when increasing the viscous damping value from $c_n = 200$ kg/s to $c_n = 800$ kg/s.

5 Conclusions

Real-time hybrid simulation was applied to the parametric exploration of the design space for a suspension system in a strut-braced wing. The wing was taken as the physical substructure and tested in a low-speed wind tunnel under aerodynamic gust loading. The vibration absorber was simulated through a real-time feedback controller with an added feedforward block, and its response at the interface with the physical substructure was imposed via an electro-mechanical linear actuator attached at the root of the strut. This set-up allowed the virtual testing of several device configurations with a single test set-up, while at the same time assessing their effect on the wing in realistic operational conditions.

As the wing response depends on its instantaneous geometric configuration in the flow, the electro-mechanical subsystem was studied in detail to assess and minimise errors at the physical interface with the wing. The assumptions related to traditional hybrid testing, where heavy-duty actuation systems are used and frequently modelled as pure delays, were found not to be applicable in general to the testing of light-weight structures

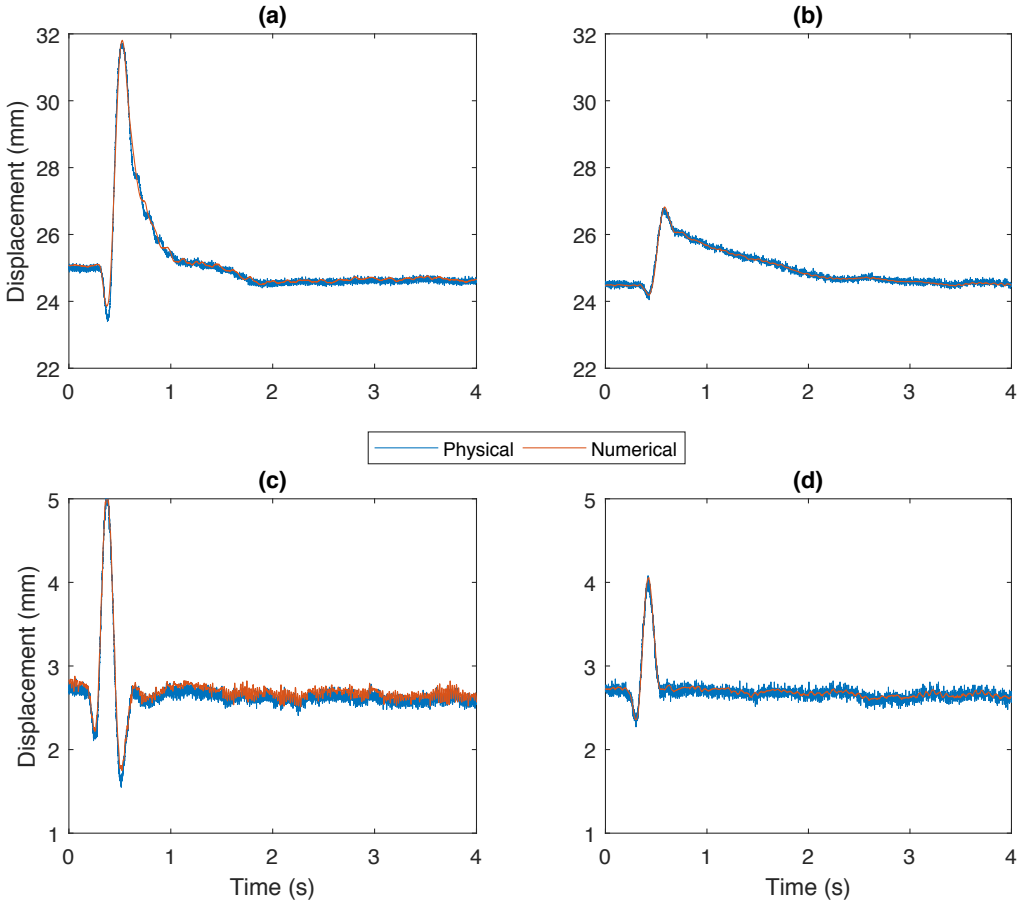

Fig. 12 Displacement response at the strut root to single gust excitation, 5 Hz, compensator activated: a) $k_n = 100$ N/m, $c_n = 200$ kg/s; b) $k_n = 100$ N/m, $c_n = 800$ kg/s; c) $k_n = 8000$ N/m, $c_n = 200$ kg/s; b) $k_n = 8000$ N/m, $c_n = 800$ kg/s.

with electromechanical actuators. The behaviour of the electro-mechanical subsystem showed a strong dependence on the characteristics of the numerical substructure and the frequency of excitation. Depending on the simulated damping, in particular, the physical system without compensation was found to exhibit either lags or leads with respect to the numerical substructure.

An outer-loop compensator based on an inverse model of the electro-mechanical subsystem alone was developed and shown to significantly reduce synchronisation errors at the interface up to 10 Hz. At higher frequencies, on the other hand, the compensator was found to be highly sensitive to uncertainties in its parameters.

The proposed approach was verified on a model strut-braced wing, which was tested in a low-speed wind tunnel and subjected to gust loading. A narrow-band implementation of the compensator was chosen in light of the absence of significant multi-harmonic components in the response of the wing. The compensator produced an excellent agreement up to 7 Hz between the displacements of the physical and numerical substructures. Between 7 and 11 Hz, the quality of the compensation less good, but still constituted an improvement over the uncompensated behaviour. The accuracy at the interface was reflected in the performance of the hybrid test as a whole: the set-up was shown to closely emulate the target vibration-suppressing device, with differences arising between 7 and 11 Hz, while the uncompensated behaviour was found to be entirely non-representative.

Acknowledgements The research presented in this work has been funded by EPSRC grant number EP/R006768/1, and the relevant data is openly available from the University of Bristol repository at https://TBD.

References

1. "Strategic Research & Innovation Agenda," tech. rep., ACARE - Advisory Council for Aviation Research and Innovation in Europe, February 2017.
2. P. M. Smith, J. DeYoung, W. A. Lovell, J. E. Price, and G. F. Washburn, "A study of high-altitude manned

research aircraft employing strut-braced wings of high-aspect-ratio," Tech. Rep. NASA-CR-159262, NASA, February 1981.

3. M. K. Bradley, C. K. Droney, and T. J. Allen, "Subsonic Ultra Green Aircraft Research. Phase II - Volume I; Truss braced wing design exploration," Tech. Rep. NASA-CR-2015-218704/VOL1, NASA, April 2015.
4. R. V. Turriziani, W. A. Lovell, G. L. Martin, J. E. Price, E. E. Swanson, and G. F. Washburn, "Preliminary design characteristics of a subsonic business jet concept employing an aspect ratio 25 strut braced wing," Tech. Rep. NASA-CR-159361, NASA, October 1980.
5. C. Szczyglowski, S. Neild, B. Titurus, J. Jiang, J. Cooper, and E. Coetzee, "Passive gust loads alleviation in a truss-braced wing using integrated dampers," in *17th International Forum on Aeroelasticity and Structural Dynamics, IFASD 2017*, 2017.
6. C. Szczyglowski, S. Neild, B. Titurus, J. Jiang, and E. Coetzee, "Passive gust load alleviation in a truss-braced wing using an inerter-based device," in *AIAA/ASCE/AHS/ASC Structures, Structural Dynamics, and Materials Conference, 2018*, 2018.
7. R. Cook, D. Calderon, M. H. Lowenberg, S. Neild, J. E. Cooper, and E. Coetzee, "Worst case gust prediction of highly flexible wings," in *58th AIAA/ASCE/AHS/ASC Structures, Structural Dynamics, and Materials Conference*, 2017.
8. R. E. Bartels, R. C. Scott, C. J. Funk, T. J. Allen, and B. W. Sexton, "Computed and experimental flutter/LCO onset for the Boeing truss-braced wing wind tunnel model," in *44th AIAA Fluid Dynamics Conference*, 2014.
9. R. G. Cook, C. Wales, A. Gaitonde, D. Jones, and J. E. Cooper, "Efficient modelling of a nonlinear gust loads process for uncertainty quantification of highly flexible aircraft," in *2018 AIAA/ASCE/AHS/ASC Structures, Structural Dynamics, and Materials Conference*, 2018.
10. P. B. Shing, "Real-time hybrid testing techniques," in *Modern Testing Techniques for Structural Systems* (O. Bursi and D. Wagg, eds.), vol. 502 of *CISM International Centre for Mechanical Sciences*, Springer-Verlag Wien, 2008.
11. D. Wagg, S. Neild, and P. Gawthrop, "Real-time testing with dynamic substructuring," in *Modern Testing Techniques for Structural Systems* (O. Bursi and D. Wagg, eds.), vol. 502 of *CISM International Centre for Mechanical Sciences*, Springer-Verlag Wien, 2008.
12. M. Nakashima, H. Kato, and E. Takaoka, "Development of real-time pseudo dynamic testing," *Earthquake Engineering & Structural Dynamics*, vol. 21, no. 1, pp. 79–92, 1992.
13. C. A. Whyte and B. Stojadinovic, "Effect of ground motion sequence on response of squat reinforced concrete shear walls," *Journal of Structural Engineering*, vol. 140, no. 8, 2014.
14. C. Kolay, J. M. Ricles, T. M. Marullo, A. Mahvashmohammadi, and R. Sause, "Implementation and application of the unconditionally stable explicit parametrically dissipative kr-α method for real-time hybrid simulation," *Earthquake Engineering & Structural Dynamics*, vol. 44, no. 5, pp. 735–755, 2015.
15. M. Wallace, D. Wagg, S. Neild, P. Bunniss, N. Lieven, and A. Crewe, "Testing coupled rotor blade-lag damper vibration using real-time dynamic substructuring," *Journal of Sound and Vibration*, vol. 307, no. 3, pp. 737 – 754, 2007.
16. A. Gonzalez-Buelga, D. J. Wagg, and S. A. Neild, "Parametric variation of a coupled pendulum-oscillator system using real-time dynamic substructuring," *Structural Control and Health Monitoring*, vol. 14, no. 7, pp. 991–1012, 2007.
17. M. L. Brodersen, G. Ou, J. Høgsberg, and S. Dyke, "Analysis of hybrid viscous damper by real time hybrid simulations," *Engineering Structures*, vol. 126, pp. 675 – 688, 2016.
18. S. J. Dyke, B. F. Spencer, P. Quast, and M. K. Sain, "Role of control-structure interaction in protective system design," *Journal of Engineering Mechanics*, vol. 121, no. 2, pp. 322–338, 1995.
19. A. Maghareh, C. E. Silva, and S. J. Dyke, "Servo-hydraulic actuator in controllable canonical form: Identification and experimental validation," *Mechanical Systems and Signal Processing*, vol. 100, pp. 398 – 414, 2018.
20. Z. Tang, M. Dietz, Z. Li, and C. Taylor, "The performance of delay compensation in real-time dynamic substructuring," *Journal of Vibration and Control*, vol. 24, no. 21, pp. 5019–5029, 2018.
21. M. I. Wallace, J. Sieber, S. A. Neild, D. J. Wagg, and B. Krauskopf, "Stability analysis of real-time dynamic substructuring using delay differential equation models," *Earthquake Engineering & Structural Dynamics*, vol. 34, no. 15, pp. 1817–1832, 2005.
22. T. Horiuchi, M. Inoue, T. Konno, and Y. Namita, "Real-time hybrid experimental system with actuator delay compensation and its application to a piping system with energy absorber," *Earthquake Engineering & Structural Dynamics*, vol. 28, no. 10, pp. 1121–1141, 1999.
23. M. Wallace, D. Wagg, and S. Neild, "An adaptive polynomial based forward prediction algorithm for multi-actuator real-time dynamic substructuring," *Proceedings of the Royal Society A: Mathematical, Physical and Engineering Sciences*, vol. 461, no. 2064, pp. 3807–3826, 2005.
24. G. A. Fermandois and B. F. Spencer, "Model-based framework for multi-axial real-time hybrid simulation testing," *Earthquake Engineering and Engineering Vibration*, vol. 16, pp. 671–691, Oct 2017.
25. S. Hayati and W. Song, "Design and performance evaluation of an optimal discrete-time feedforward controller for servo-hydraulic compensation," *Journal of Engineering Mechanics*, vol. 144, no. 2, p. 04017163, 2018.
26. A. Bartl, J. Mayet, M. K. Mahdiabadi, and D. J. Rixen, "Multi-DoF interface synchronization of real-time-hybrid-tests using a recursive-least-squares adaption law: A numerical evaluation," in *Dynamics of Coupled Structures, Volume 4* (M. Allen, R. L. Mayes, and D. Rixen, eds.), (Cham), pp. 7–14, Springer International Publishing, 2016.
27. V. Chabaud, S. Steen, and R. Skjetne, "Real-time hybrid testing for marine structures: Challenges and strategies," in *ASME. International Conference on Offshore Mechanics and Arctic Engineering, Volume 5: Ocean Engineering*, 2013.
28. A. W. Mackowski and C. H. Williamson, "Developing a cyber-physical fluid dynamics facility for fluid–structure interaction studies," *Journal of Fluids and Structures*, vol. 27, no. 5, pp. 748 – 757, 2011. IUTAM Symposium on Bluff Body Wakes and Vortex-Induced Vibrations (BBVIV-6).
29. F. Hover, S. Miller, and M. Triantafyllou, "Vortex-induced vibration of marine cables: Experiments using force feedback," *Journal of Fluids and Structures*, vol. 11, no. 3, pp. 307 – 326, 1997.

30. E. M. Garcia and M. M. Bernitsas, "Effect of damping on variable added mass and lift of circular cylinders in vortex-induced vibrations," *Journal of Fluids and Structures*, vol. 80, pp. 451 – 472, 2018.
31. K. Onoue, A. Song, B. Strom, and K. S. Breuer, "Large amplitude flow-induced oscillations and energy harvesting using a cyber-physical pitching plate," *Journal of Fluids and Structures*, vol. 55, pp. 262 – 275, 2015.
32. C. Fagley, J. Seidel, and T. McLaughlin, "Cyber-physical flexible wing for aeroelastic investigations of stall and classical flutter," *Journal of Fluids and Structures*, vol. 67, pp. 34 – 47, 2016.
33. C. P. Fagley, D. Broadbent, J. Seidel, and T. E. McLaughlin, "Stall flutter prediction and experimental verification using a cyber-physical wing," in *55th AIAA Aerospace Sciences Meeting*, 2017.
34. T. Sauder, S. Marelli, K. Larsen, and A. J. Sørensen, "Active truncation of slender marine structures: Influence of the control system on fidelity," *Applied Ocean Research*, vol. 74, pp. 154 – 169, 2018.
35. T. Sauder, S. Marelli, and A. J. Sørensen, "Probabilistic robust design of control systems for high-fidelity cyber–physical testing," *Automatica*, vol. 101, pp. 111 – 119, 2019.
36. R. Waghela, M. Bryant, and F. Wu, "Control design in cyber-physical fluid–structure interaction experiments," *Journal of Fluids and Structures*, vol. 82, pp. 86 – 100, 2018.
37. C. Wales, R. Cook, D. Jones, and A. Gaitonde, "Comparison of aerodynamic models for 1-cosine gust loads prediction," in *17th International Forum on Aeroelasticity and Structural Dynamics, IFASD 2017*, 2017.
38. C. Howcroft, R. G. Cook, S. A. Neild, M. H. Lowenberg, J. E. Cooper, and E. B. Coetzee, "On the geometrically exact low-order modelling of a flexible beam: formulation and numerical tests," *Proceedings of the Royal Society A: Mathematical, Physical and Engineering Sciences*, vol. 474, no. 2216, p. 20180423, 2018.
39. F. Afonso, J. Vale, E. Oliveira, F. Lau, and A. Suleman, "A review on non-linear aeroelasticity of high aspect-ratio wings," *Progress in Aerospace Sciences*, vol. 89, pp. 40 – 57, 2017.
40. N. Terkovics, S. A. Neild, M. Lowenberg, R. Szalai, and B. Krauskopf, "Substructurability: the effect of interface location on a real-time dynamic substructuring test," *Proceedings of the Royal Society A: Mathematical, Physical and Engineering Sciences*, vol. 472, no. 2192, p. 20160433, 2016.
41. S. Hoffait, F. Marin, D. Simon, B. Peeters, and J.-C. Golinval, "Measured-based shaker model to virtually simulate vibration sine test," *Case Studies in Mechanical Systems and Signal Processing*, vol. 4, pp. 1 – 7, 2016.
42. J. Kennedy and R. Eberhart, "Particle swarm optimization," in *Proceedings of ICNN'95 - International Conference on Neural Networks*, vol. 4, pp. 1942–1948, Nov 1995.
43. B. M. Phillips and B. F. Spencer, "Model-based multiactuator control for real-time hybrid simulation," *Journal of Engineering Mechanics*, vol. 139, no. 2, pp. 219–228, 2013.
44. H. Zhou, D. J. Wagg, and M. Li, "Equivalent force control combined with adaptive polynomial-based forward prediction for real-time hybrid simulation," *Structural Control and Health Monitoring*, vol. 24, no. 11, 2017.
45. K. T. Wood, R. C. Cheung, T. S. Richardson, J. E. Cooper, O. Darbyshire, and C. Warsop, "A new gust generator for a low speed wind tunnel: Design and commissioning," in *55th AIAA Aerospace Sciences Meeting*, 2017.
46. C. Neuman and C. Baradello, "Digital transfer functions for microcomputer control," *IEEE Transactions on Systems, Man, and Cybernetics*, vol. 9, pp. 856–860, Dec 1979.